

Topological surface states in thick partially relaxed HgTe filmsM. L. Savchenko,^{1,2} D. A. Kozlov,^{1,2} N. N. Vasilev,^{1,2} Z. D. Kvon,^{1,2} N. N. Mikhailov,^{1,2}
S. A. Dvoretzky,² and A. V. Kolesnikov²¹*Novosibirsk State University, Physics Department, Novosibirsk 630090, Russia*²*Rzhanov Institute of Semiconductor Physics, Novosibirsk 630090, Russia*

(Received 9 November 2018; published 14 May 2019)

Surface states of topological insulators (TIs) have been playing the central role in the majority of outstanding investigations in low-dimensional electron systems for more than 10 years. TIs based on high-quality strained HgTe films demonstrate a variety of subtle physical effects. The strain leads to a bulk band gap but limits a maximum HgTe strained film thickness, and therefore, the majority of experiments were performed on films with a thickness of less than 100 nm. Since a spatial separation of topological states is crucial for the study of a single-surface response, it is essential to increase the HgTe thickness further. In this work, by combining transport measurements together with capacitance spectroscopy, we perform an analysis of a 200-nm partially relaxed HgTe film. The Drude fit of the classical magnetotransport reveals the ambipolar electron-hole transport with a high electron mobility. A detailed analysis of Shubnikov–de Haas oscillations in both conductivity and capacitance allows us to distinguish three groups of electrons, identified as electrons on top and bottom surfaces and bulk electrons. The indirect bulk energy gap value is found to be close to zero. It is established that the significant gap decrease does not affect the surface states, which are found to be well resolved and spin nondegenerate. The presented techniques allow investigations of other three-dimensional TIs, regardless of the presence of bulk conductivity.

DOI: [10.1103/PhysRevB.99.195423](https://doi.org/10.1103/PhysRevB.99.195423)**I. INTRODUCTION**

An ideal three-dimensional topological insulator (3D TI) is a system that has spin-nondegenerate surface states with spin-momentum locking and insulating bulk [1]. The unique properties of 3D TIs result in many unique physical effects: spin polarization of the 3D TI current [2], 4π oscillations in a superconductor contact [3], a universal magnetoelectric effect [4], and Majorana fermions [5]. The existence of the mentioned surface states was established in Bi- and Sb-based and HgTe 3D TIs by means of angle-resolved photoemission spectroscopy [6–9]. Then they were studied in magneto-optic [4,10,11] and magnetotransport experiments [9,12–15] and by magnetocapacitance spectroscopy [16].

There are several issues hampering the investigation of the surface states. The main shortcoming of Bi- and Sb-based 3D TIs is a crystalline imperfection leading to intrinsic doping and reduced carrier mobility. Even recently, the fabrication of samples with pure surface conductivity was difficult to implement, and one either had to study a transport response of the surface states intermixed with the bulk ones [17–20] or had to use other techniques, e.g., studying photogalvanic effects involving a space symmetry analysis [21], which allowed distinguishing the bulk and surface carriers. Although, in recent papers, the surface-dominant conductivity was conclusively shown [22–25], the best samples still have significant disorder, smearing fine effects: for instance, a pronounced quantum Hall effect plateau requires a magnetic field close to or even exceeding the limit of superconductive magnets [23–25].

In contrast, strained HgTe-based 3D TIs are characterized by much smaller disorder and higher electron mobility values

exceeding $10^5 \text{ cm}^2/\text{Vs}$ [14]. Moreover, the highest quality of such systems allowed studying delicate ballistic and interference effects [15,26]. However, these systems have their own shortcomings, mainly coming from a zero-energy gap in bulk HgTe. In order to open the gap and organize a 3D TI, one has to apply a strain: HgTe films, grown on a CdTe substrate with a 0.3% lattice mismatch, have an indirect band gap of 15 meV. In turn, the requirement of the strain limits the maximum HgTe film thickness to about 100–150 nm because of its relaxation at higher thicknesses (according to [9] and our experience). This fact explains why in the majority of papers devoted to the HgTe-based 3D TIs only 70–100-nm films were studied [3,9,14,15,26–29]. On the other hand, studying thicker HgTe films is also desirable because of the higher separation between the surface states, weaker mutual electrostatic coupling, and possible hybridization. One could expect that the thicker films would be partially or fully relaxed, resulting in a smaller or even zero effective energy gap. In such a system the bulk carriers would inevitably appear at all Fermi level positions. Based on the above, the issue of surface and bulk state coexistence seems to be real. Moreover, there are some materials predicted to have a nontrivial topology with the lack of a band gap or with band overlapping [30,31].

In this paper, we investigate 200-nm HgTe films that can be characterized by the partial strain. The samples under investigation are equipped with a metallic top gate allowing us to widely vary a Fermi level position from the valence to conduction bands. By combining classical and quantum magnetotransport studies, as well as magnetocapacitance spectroscopy, we show that neither a significant decrease in the bulk gap nor the presence of trivial bulk conductivity affects

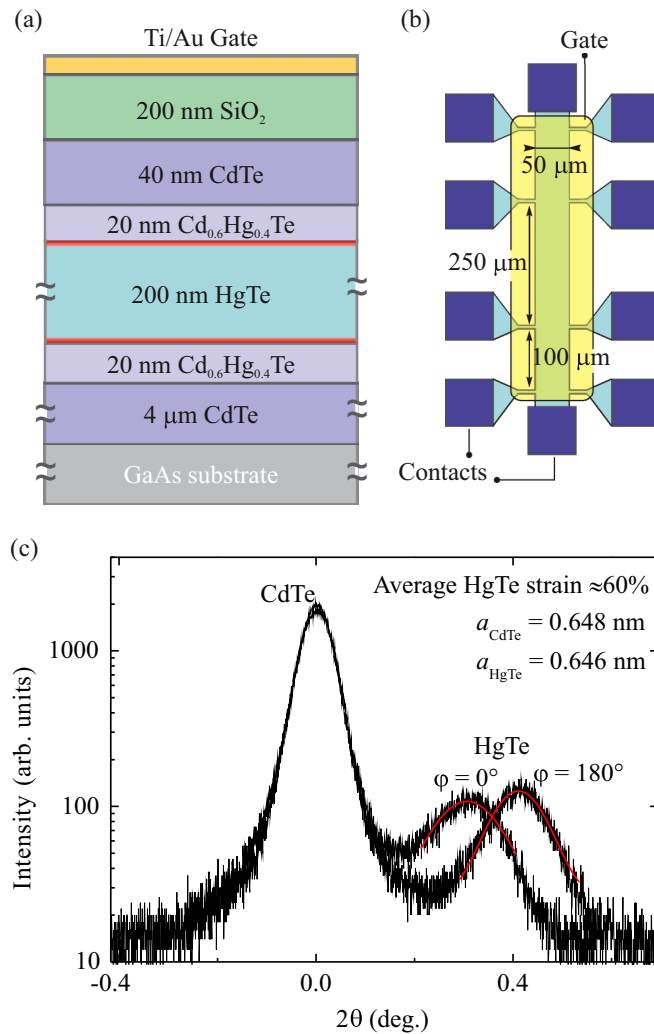


FIG. 1. (a) Schematic cross section of the structure under study. The 200-nm HgTe film is sandwiched between thin Cd_{0.6}Hg_{0.4}Te buffer layers covered by a 200-nm SiO₂ insulator and a metallic gate. Bright red lines represent the surface states on the top and bottom surfaces of the film. (b) Schematic top view of the studied Hall bars. (c) X-ray diffraction curves of the system obtained in opposite directions for a [026] reflex (for azimuth angles $\varphi = 0^\circ$ and 180°). The HgTe peak positions relative to CdTe allow determining its average strain, which is about 60% (100% means that the HgTe film has the CdTe lattice constant and a 15 meV indirect bulk band gap; 0% means that it is fully relaxed to its own lattice constant and has some meV of the bands overlap [32]).

the surface states. A detailed analysis reveals the main properties of the surface and bulk carriers and proves that the surface states are still spin nondegenerate.

II. EXPERIMENTAL DETAILS

All measurements are carried out on 200-nm HgTe films that have been grown by molecular beam epitaxy on a GaAs(013) substrate with the same layer ordering as for the usual 80-nm films [14].

In Fig. 1(a) we schematically show a cross-section view of the system under study. The 200-nm HgTe film is sandwiched

between thin Cd_{0.6}Hg_{0.4}Te barriers, and a Ti/Au gate has been deposited on the 200-nm SiO₂ insulator grown by a low-temperature chemical vapor deposition process.

The approximate thickness of the pseudomorphic growth of a HgTe film on a CdTe substrate with a 0.3% larger lattice constant is about 100–150 nm (according to [9] and our experience). The full 100% adoption of the CdTe substrate lattice constant results in a uniaxial strain and opening of an indirect 15 meV bulk band gap [10]. To reveal the crystalline perfection of the grown 200-nm HgTe structure, a two-crystal x-ray diffractometer was used [Cu K_α radiation with a Ge (400) monochromator]. Shown in Fig. 1(c) are the high-resolution diffraction curves of a [026] reflex in a symmetrical Bragg geometry. The data confirm the suggested relaxation, but it is not full: the structure still adopts the CdTe lattice constant, which is an average of bulk CdTe and HgTe with weights of 60% and 40%, respectively. Compared with thinner (with thickness below 100 nm) HgTe films, the film under study is only 60% strained [33]. In turn, the reduced strain should lead to a smaller value of the band gap. The following transport measurements show nearly a zero indirect band gap.

Several Hall-bar samples were prepared from one wafer, showing similar results. For the consistency of magnetotransport and capacitance responses, all the presented data are from one sample. In Fig. 1(b) we show a schematic top view of the studied Hall bars with a 50-μm current channel and 100- and 250-μm distances between potential probes. In order to enhance the signal-to-noise ratio during the capacitance measurements, the gate covered not only the central part of the Hall bar but a significant part of the contact leads as well. The total area of the gated region was around 1.1 mm². Transport measurements were performed using a standard lock-in technique with a driving current in the range of 10^{-7} – 10^{-8} A in a perpendicular magnetic field B up to 12 T at a temperature of 0.2 K. A typical frequency for transport measurements was 12 Hz, which was decreased to 2 Hz in the case of high magnetic fields. For the capacitance measurements we mixed the dc bias V_g with a small ac voltage V_{ac} and measured the ac current flowing across our device phase sensitively. The total capacitance measured in such a way between the metallic top gate and a 2D electron system (2DES) depends, in addition to the geometric capacitance, on the quantum capacitance e^2D , connected in series and reflecting the finite density of states D of the 2DES [16,34]; e is the elementary charge, and D is the thermodynamic density of states. The ac frequency for capacitance measurements was in the range of 2–680 Hz. The frequency independence of measured resistance and capacitance C was controlled, excluding both the existence of leakage currents and resistive effects. The parasitic capacitance of our setup was about 40 pF.

III. RESULTS AND DISCUSSION

A detailed analysis of the magnetotransport and capacitance data reveals the following main idea: the spin-nondegenerate surface states, originating from the HgTe inverted band structure, persist in the 200-nm partially relaxed film and act in a way very similar to those in strained films with bulk gaps. Like they are for 80-nm HgTe films [14,16],

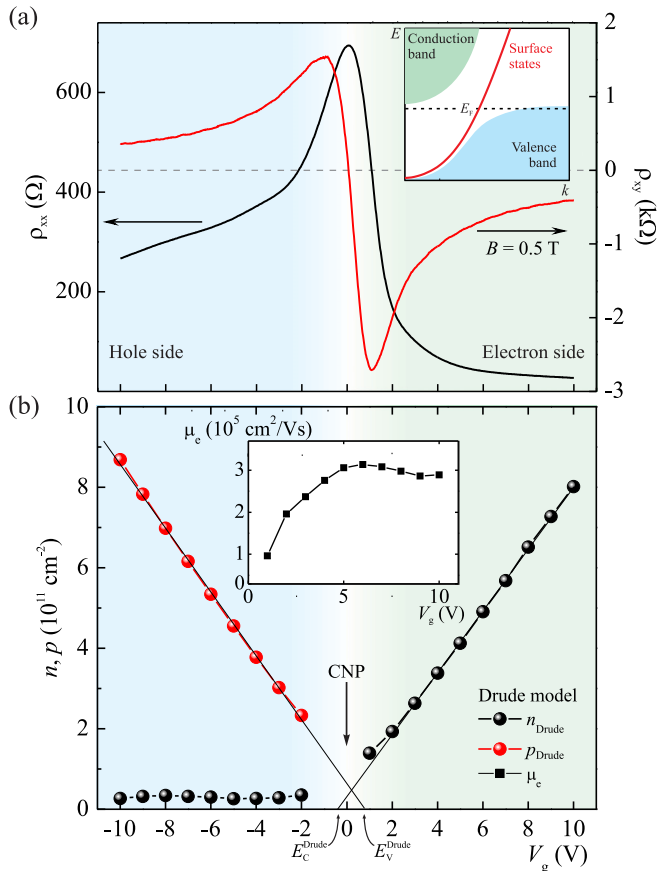


FIG. 2. (a) The gate dependences of longitudinal resistivity ρ_{xx} (measured at zero magnetic field, black line) and Hall resistance ρ_{xy} (at magnetic field $B = 0.5$ T, red line). ρ_{xx} exhibits its maximum, while ρ_{xy} changes sign in the vicinity of a charge neutrality point of the system. Inset: a schematic band diagram of the system at zero gate voltage. (b) The gate voltage dependences of the total electron n_{Drude} (black spheres) and hole p_{Drude} (red spheres) densities obtained from the two-component Drude model fitting of the $\rho_{xx}(B)$ and $\rho_{xy}(B)$ traces. The linear extrapolation of p_{Drude} and n_{Drude} to zero values results in the highlighting of two points on the V_g axis for holes and electrons, respectively, marked as E_V^{Drude} at $V_g \approx 0.8$ V and E_C^{Drude} at $V_g \approx -0.3$ V. The first point corresponds to the state of the system when the Fermi level touches the top of the valence band. However, the second point has only a virtual meaning without any well-defined state of the system (see text for details). Inset: the gate dependence of the average electron mobility μ_e at positive gate voltages.

the surface carriers of the system are high-mobility electrons, while in the bulk one can observe both electrons and holes depending on the Fermi level position.

In the inset of Fig. 2(a) we show a suggested schematic band diagram of the system at zero gate voltage. In terms of band structure, the partially relaxed 200-nm film behaves like an intermediate between an 80-nm film [14] and bulk HgTe [32]. While the conduction band has its minimum at the Γ point, the top of the valence band is situated beside the Brillouin zone center with an indirect energy bulk gap of around 3 meV. The band inversion symmetry of the system results in the formation of the topological surface states [1]

[shown in red in Fig. 2(a)] with linearlike dispersion and the Dirac point located deep in the valence band [9].

A. Classical transport and Drude fitting

Shown in Fig. 2(a) are the typical resistivity ρ_{xx} at magnetic field $B = 0$ and Hall resistance ρ_{xy} at $B = 0.5$ T as functions of gate voltage V_g at $T = 0.2$ K. The ρ_{xx} trace exhibits a maximum near $V_g = 1$ V and is asymmetric with respect to V_g : the resistivity on the left side of the maximum is significantly higher than that on the right side. In the vicinity of the $V_g = 0$ V point ρ_{xy} changes sign. The obtained behavior is very similar to the observed one in thinner HgTe films [14] and in line with the expectations that the gate voltage changes the position of the Fermi level from the valence to conduction band. On the right side of the peak, where ρ_{xy} is negative, the Fermi level goes to the conduction band, and the carriers are the high-mobility surface electrons and moderate-mobility bulk ones. In this region ρ_{xx} reaches its minimal values. At negative gate voltages, the Fermi level goes to the valence band, where the bulk holes and the surface electrons coexist, resulting in a nonlinear sign-variable Hall effect similar to what was observed in 80-nm films [14] (not shown). An almost one order difference in ρ_{xx} values between the left and right sides of the resistivity peak indicates a significant difference in electron and hole mobilities.

In order to obtain the values of electron and hole densities and mobilities (n_{Drude} and p_{Drude} and μ_e and μ_p , respectively) we used the two-component Drude model fitting of both $\rho_{xx}(B)$ and $\rho_{xy}(B)$ dependences at fixed gate voltages, as carried out in our earlier works [14,35]. One should note that, practically, there is more than one kind of electron in the system, namely, two kinds of surface electrons (from the top and bottom surfaces) and the bulk carriers. However, the tolerance of the Drude model does not allow distinguishing between them. Therefore, the values of n_{Drude} and $\mu_e(V_g)$, obtained from the fitting, reveal the total electron density and the average electron mobility. The $n_{\text{Drude}}(V_g)$ and $p_{\text{Drude}}(V_g)$ density dependences obtained in this manner are shown in Fig. 2(b). The mobility dependence $\mu_e(V_g)$ for the region $V_g > 0$ is shown in the inset. On the negative-gate-voltage side, where the bulk holes and surface electrons coexist, the performed fitting provides both densities but only the hole mobility, while the electron mobility remains uncertain. The hole mobility is proved to be gate independent and has a value of about $10^4 \text{ cm}^2/\text{V s}$ (not shown).

The density dependences obtained from the Drude fitting can be interpreted in the following way. At zero gate voltage the Fermi level is located near the top of the valence band, where the bulk holes coexist with nearly the same number of electrons, presumably the surface ones. By applying small positive V_g the total electron density $n_{\text{Drude}}(V_g)$ increases, although not with the full filling rate because of the presence of the bulk hole. At $V_g = E_V^{\text{Drude}}$ [see the caption of Fig. 2(b)] the Fermi level touches the top of the valence band. At $V_g > E_V^{\text{Drude}}$ the bulk holes disappear, while the electron density n_{Drude} increases linearly with V_g with the full filling rate. On the contrary, by applying negative V_g one mainly increases p_{Drude} , while $n_{\text{Drude}}(V_g)$ stays almost constant because of much smaller effective mass values and hence those of the density of

states. A small increase in $n_{\text{Drude}}(V_g)$ observed at $V_g < -5$ V has no physical sense and probably indicates a fitting uncertainty in this range. The total filling rate dn/dV_g describes the change in the total carrier density ($n_{\text{Drude}} - p_{\text{Drude}}$) with V_g and is mainly determined by the insulator layer sequence. The filling rate obtained from the experiment is found to be $8.0 \times 10^{10} \text{ cm}^{-2}/\text{V}$, which is in line with electrostatic calculations.

One should note that the Drude fitting gives only the total electron density value and not partial ones. Therefore, the Drude fitting does not reveal the actual position of the bottom of the conduction band. The E_C^{Drude} point on the V_g axis obtained from a linear extrapolation does not correspond to any well-defined state of the system and has only a virtual sense. Consequently, it is impossible to extract the bulk energy gap value from the classical magnetotransport data. More information can be obtained only from an analysis of the quantum oscillations.

B. Quantum transport and capacitance oscillations

In contrast to the classical transport, the analysis of Shubnikov–de Haas (SdH) oscillations in systems with high enough quantum mobility allows determining the partial densities of all carriers [14,36]. One can expect four groups of carries in the system under study, although at $V_g > E_V^{\text{Drude}}$ only three of them are left. Each group of carriers is characterized by a density giving its own frequency of the SdH oscillations on a $1/B$ scale. The issue of carrier identification from the resistivity oscillations with three kinds of electrons in a general case looks rather complicated, and its solution is too ambiguous. On the other hand, the issue can be simplified if one complements the resistivity oscillations with the capacitance ones. In the case of an ordinary 2DES the capacitance oscillations simply reflect the density of states modulation by a magnetic field. However, in the case of an essentially thick film with several groups of carriers that are located at different areas across the film, it turns out that the amplitude of the capacitance oscillations produced by each group is in the inverse relation with distance from the carriers to the gate [16,37]. Therefore, one can expect that the amplitude of the SdH oscillations observed in capacitance induced by the top surface electrons is the most enhanced, while the electrons on the bottom surface, being the most distant from the gate, produce oscillations with a suppressed amplitude. Through a comparison of the oscillations in capacitance and transport and their Fourier spectra, measured at the same conditions, one can identify what is what.

In Fig. 3 we show the normalized SdH conductivity oscillations $\Delta\sigma_{xx}/\sigma_{xx}^0$ at different gate voltages [Figs. 3(a) and 3(b)] vs a reciprocal magnetic field B^{-1} , the gate dependence of measured capacitance $C(V_g)$ at zero and nonzero magnetic fields [Fig. 3(c)], and its oscillations $\Delta C(B^{-1})$ for different V_g values [Fig. 3(d)]. Each oscillation pattern in the B^{-1} scale was subject to a fast Fourier transform (FFT) analysis (see the Appendix for details).

On the hole side of the gate voltages the SdH oscillations [Fig. 3(a)] demonstrate the simplest pattern, and their Fourier spectra demonstrate two well-defined peaks [see Fig. 4(a)]. The behavior is typical for 2D systems, where high-mobility

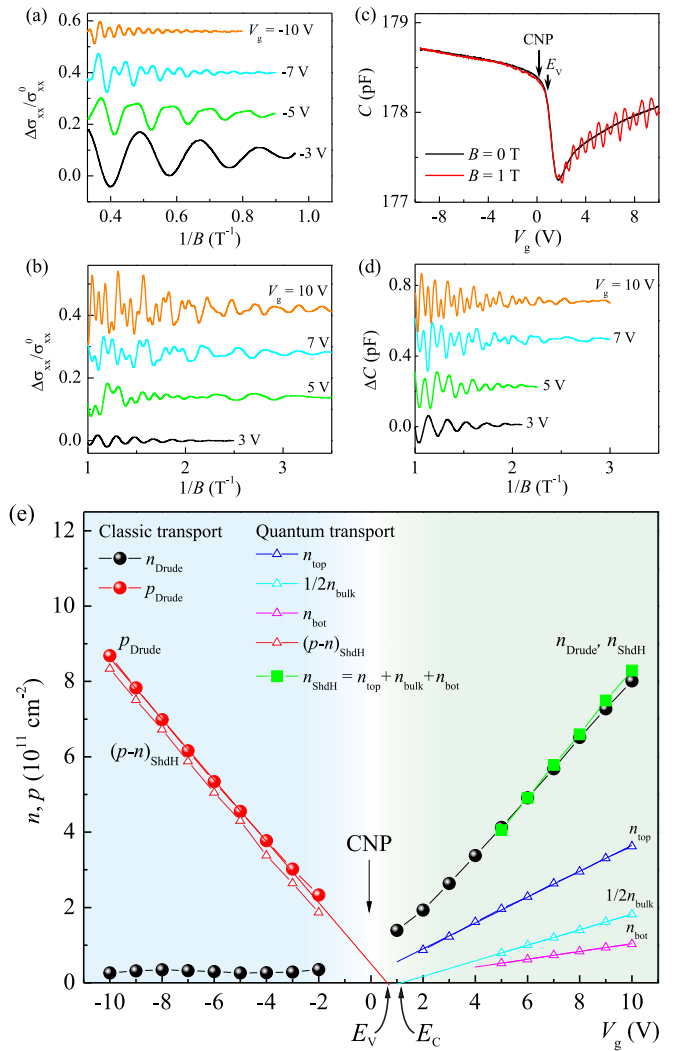


FIG. 3. (a) and (b) The normalized conductivity oscillations $\Delta\sigma_{xx}/\sigma_{xx}^0 = (\sigma_{xx} - \langle\sigma_{xx}\rangle)/\sigma_{xx}^0$ on the B^{-1} scale for the hole and electrons sides, respectively, where $\langle\sigma_{xx}\rangle$ denotes the monotonous part of σ_{xx} and $\sigma_{xx}^0 \equiv \sigma_{xx}(B=0)$. (c) The gate dependences of the capacitance $C(V_g)$ measured at zero magnetic field (black line) and at $B = 1$ T (red line). (d) The SdH oscillations in $\Delta C = C - C(B=0)$ for the electron side. (e) The combined gate voltage density dependences obtained from both classical transport and SdH oscillation analyses. n_{Drude} and p_{Drude} have the same color code as in Fig. 2(b) and are shown as black and red spheres, respectively. From SdH oscillations the following densities were obtained: the differential density $(p-n)_{\text{SdH}}$ for the hole side and partial densities n_{top} , n_{bulk} , and n_{bot} for the electron side. The $\frac{1}{2}n_{\text{bulk}}$ is shown for consistency with a FFT spectral analysis. Also the total electron density, obtained as $n_{\text{SdH}} = n_{\text{top}} + n_{\text{bulk}} + n_{\text{bot}}$, is shown by green squares.

and low-density electrons coexist with low-mobility and high-density holes. Because of their low density, the electrons do not produce any well-resolved peaks in the Fourier spectrum. In contrast, the holes induce the SdH oscillations accompanied by two well-resolved peaks in the FFT spectrum of frequencies f_1^h and f_2^h . For every gate voltage these frequencies are governed by the relation $2f_1^h = f_2^h$ [see Fig. 4(b)] and

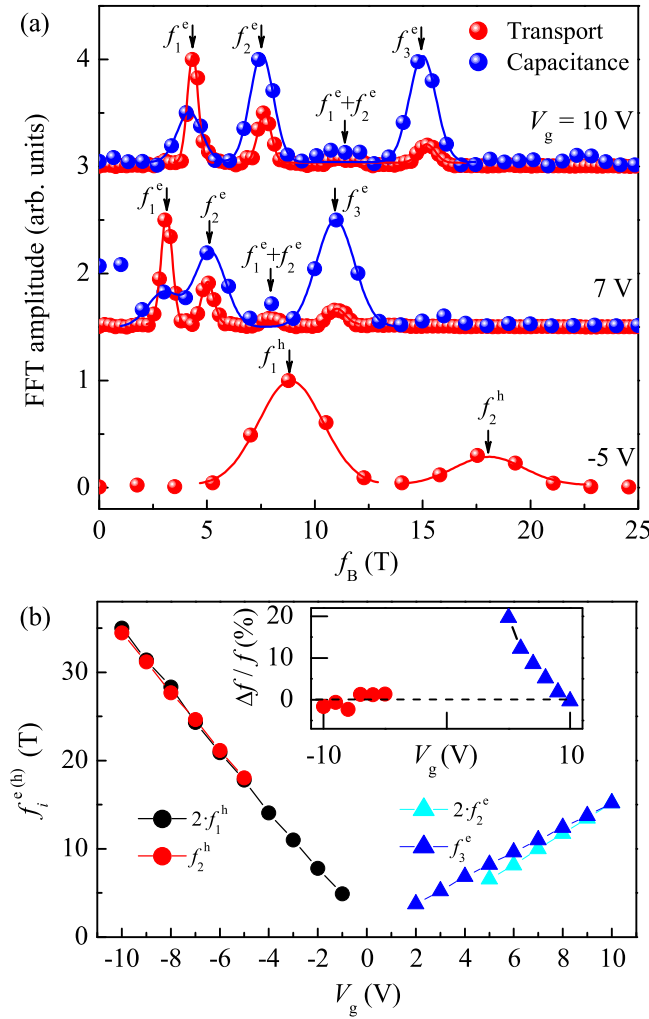


FIG. 4. (a) The typical Fourier spectra of the conductivity (red spheres) and capacitance (blue spheres) SdH oscillations at different fixed gate voltages. The solid lines correspond to the fitting by Gaussian functions. The vertical arrows point out the central frequency of each Gaussian fit. (b) The ratio between positions of different peaks. On the hole side $2f_1^h(V_g)$ (black circles) closely follows the $f_2^h(V_g)$ (red circles) dependence, indubitably pointing out their common origin, namely, spin-degenerate and spin-resolved Landau levels of bulk holes, respectively. In contrast, on the electron side the $2f_2^e(V_g)$ (cyan triangles) and $f_3^e(V_g)$ (blue triangles) dependences demonstrate different slopes, indicating the different natures of the peaks characterized by these frequencies. Inset: the enhanced difference between hole $(f_2^h - 2f_1^h)/f_2^h$ (red circles) and electron $(f_3^e - 2f_2^e)/f_3^e$ (blue triangles) traces at the same values of V_g .

therefore correspond to the formation of spin-degenerate and spin-resolved bulk hole Landau levels, respectively. However, the exact frequency values correspond to the differential density $(p - n)$ and not to the hole one [14,38]. The gate voltage dependence of $(p - n)_{\text{SdH}}(V_g) = (2e/h)f_1^h$ is shown by red triangles in Fig. 3(e); h is the Planck constant. The obtained data are in full agreement with the Drude fitting since it is clearly seen that the $(p - n)_{\text{SdH}}(V_g)$ dependence accurately follows $p_{\text{Drude}}(V_g)$ with a shift of around $n_{\text{Drude}}(V_g)$, i.e., $p_{\text{Drude}}(V_g) - n_{\text{Drude}}(V_g) = (p - n)_{\text{SdH}}(V_g)$.

On the positive-gate-voltage side the SdH oscillations demonstrate a much more complicated structure in both the conductivity and capacitance [see Figs. 3(b) and 3(d)]. Because of the high electron mobility, the first oscillations appear at magnetic fields as low as 0.25 T, while at $B > 1$ T the transition to the quantum Hall state begins (not shown). Because of our focus on the SdH oscillations, we limited the magnetic field range to 1 T. For the traces measured at $V_g \geq 5$ V the Fourier spectra demonstrate three independent well-resolved peaks [see Fig. 4(a)], characterized by the frequencies of f_1^e , f_2^e , and f_3^e . Also additional peaks with frequencies of $f_1^e \pm f_2^e$ and of much smaller amplitudes are seen. A comparison of the conductivity and capacitance Fourier spectra reveals that the relative peak heights significantly differ between two techniques: the peak with frequency f_3^e is strongly enhanced in the capacitance spectra (compared to its amplitude in the corresponding transport spectra), and this points out that it stems from the top surface electrons with a density of $n_{\text{top}} = (e/h)f_3^e$ [see Fig. 3(e)]. On the contrary, the peak with the f_1^e frequency is strongly suppressed in the capacitance response, indicating that it originates from the bottom surface electrons with a density of $n_{\text{bot}} = (e/h)f_1^e$. Then, the peak with frequency f_2^e should be associated with the bulk electrons. Since the bulk electrons are expected to be spin degenerate, their density should be governed by the relation $n_{\text{bulk}} = (2e/h)f_2^e$. One should note that the spin degeneracy of the bulk carriers should be removed in strong magnetic fields. Indeed, the SdH oscillation splittings were observed in magnetic fields up to 5–12 T, but the corresponding Fourier spectra did not demonstrate a well-resolved peak with a frequency of $2f_2^e$, probably because of the proximity to the f_3^e peak. At $V_g < 5$ V the peaks with frequencies f_1^e and f_2^e become hardly visible, while the f_3^e peak persists.

Independent proof of supposed carrier identification can be obtained by a comparison of the densities, resulting from the SdH oscillations, with the total density obtained from the Drude fits. An almost perfect coincidence of $n_{\text{Drude}}(V_g)$ with $n_{\text{top}} + n_{\text{bot}} + n_{\text{bulk}}$ was obtained [see Fig. 3(e)]. All other possible correspondences of the Fourier peaks with the groups of carriers were checked, but much worse agreement in the relation $n_{\text{Drude}} = (e/h)(\sum g_i f_i^e)$ was obtained, where $g_i = 1, 2$ are possible spin degeneracy values. An additional check that $f_3^e \neq 2f_2^e$ was performed, proving that the peaks with the f_2^e and f_3^e frequencies have different origins. Indeed, as one can easily see in Fig. 4(b), the $f_3^e(V_g)$ and $2f_2^e(V_g)$ dependences have different slopes with an interception around $V_g = 10$ V, indicating their distinct origin.

Conclusively, the combined analysis of the capacitance and magnetotransport data allows distinguishing and identifying three groups of electrons. Additional information about the band structure can be obtained by a linear extrapolation of the $n_{\text{bulk}}(V_g)$ dependence [Fig. 3(e)]. Its cross section with the horizontal axis occurs at $V_g = 1.2$ V and marks E_C as a conduction band bottom. The valence band top E_V was correctly determined by the classical transport analysis and is located at $V_g = 0.8$ V. The difference between E_C and E_V defines the bulk energy gap. The obtained value of 0.4 V is 5 times smaller than in the strained HgTe films [14,16]. Therefore, one can estimate that the energy gap value in the partially relaxed HgTe film is about 2–3 meV. One should note

that the obtained indirect energy gap value has the same order as the characteristic disorder in the system.

IV. CONCLUSION

In conclusion, by combining the transport measurements with the capacitance spectroscopy, we performed an analysis of the 200-nm partially relaxed HgTe film. The Drude fit of the classical magnetotransport measurements revealed the ambipolar electron-hole transport of high electron mobility. A detailed analysis of the Shubnikov–de Haas oscillations in both conductivity and capacitance allowed distinguishing three electron groups, identified as electrons on the top and bottom surfaces and the bulk electrons. The indirect bulk energy gap value was found to be 3 meV. It has been established that a significant reduction of the bulk gap does not affect the main properties of the surface states that are found to be spin nondegenerate. The results of the work also confirm that the topological surface states are robust to the existence of trivial carriers in a quasi-three-dimensional system. The presented techniques allow investigations of other 3D TIs regardless of a bulk gap or conductance existence.

ACKNOWLEDGMENTS

This work supported by RFBR Grants No. 18-32-00138 (transport results) and No. 18-42-543013 (together with the government of the Novosibirsk Region of the Russian Federation). D.A.K. was supported by Russian President Grant No. MK-3603.2017.2.

APPENDIX: SDH OSCILLATION ANALYSIS

The analysis of Shubnikov–de Haas oscillations allows determining the carrier density at a rather high precision, but in the case of several types of carriers the procedure should be performed carefully. Here we describe how the oscillations were processed.

In the first step we measured the wide-range magnetic field dependences of the longitudinal ρ_{xx} and perpendicular ρ_{xy} components of a resistivity tensor. Then we calculated the experimental conductivity trace $\sigma_{xx}(B^{-1})$, with which it is better to work because of a smaller monotonous part but which still has to be removed. The monotonous part, denoted as $\langle\sigma_{xx}\rangle$, was obtained by the smoothing of every $\sigma_{xx}(B^{-1})$ trace with an averaging period higher than a characteristic oscillation period. Finally, the oscillatory conductivity part was normalized using the formula $\Delta\sigma_{xx}/\sigma_{xx}^0 = [\sigma_{xx}(B^{-1}) - \langle\sigma_{xx}(B^{-1})\rangle]/\sigma_{xx}(B=0)$, and it is shown in Figs. 3(a) and 3(b). The last step before the Fourier transform was shrinking the magnetic field range because small fields do not consist of any useful information, while at high fields the transition to the quantum Hall state begins. On the hole side the optimal range was found to be from 1.1 to 3 T, while on the electron side the range was limited from 0.2–0.4 to 1 T depending on the gate voltage. The maximum oscillation amplitude was about 10%–15%.

The procedure was rather similar for the capacitance traces $C(B)$. The only difference was the absence of the monotonous part, so $\Delta C(B^{-1}) = C(B^{-1}) - C(B=0)$. For the electron side the magnetic field range was limited from 0.3–0.4 to 1 T depending on the gate voltage. For the hole side the capacitance measurements were not performed.

Finally, every oscillatory trace was subjected to the fast Fourier transform. The typical spectra obtained are shown in Fig. 4(a). Each spectrum demonstrates a set of peaks which are characterized by frequencies f_i . The best known way to determine the precise f_i value, especially in the case of closely spaced peaks, is fitting each peak with any delomlike dependence. We used Gaussian functions $A_i \exp(-\frac{(f-f_i)^2}{2\Delta f^2})$ with a central frequency f_i for the fitting of each peak. The obtained fitting is shown in Fig. 4(a) by solid lines. The corresponding central frequencies are marked by vertical arrows.

-
- [1] Y. Ando, *J. Phys. Soc. Jpn.* **82**, 102001 (2013).
 [2] Y. Fan and K. L. Wang, *SPIN* **06**, 1640001 (2016).
 [3] J. Wiedenmann, E. Bocquillon, R. S. Deacon, S. Hartinger, O. Herrmann, T. M. Klapwijk, L. Maier, C. Ames, C. Brüne, C. Gould, A. Oiwa, K. Ishibashi, S. Tarucha, H. Buhmann, and L. W. Molenkamp, *Nat. Commun.* **7**, 10303 (2016).
 [4] V. Dziom, A. Shuvaev, A. Pimenov, G. V. Astakhov, C. Ames, K. Bendias, J. Böttcher, G. Tkachov, E. M. Hankiewicz, C. Brüne, H. Buhmann, and L. W. Molenkamp, *Nat. Commun.* **8**, 15197 (2017).
 [5] M. Sato and Y. Ando, *Rep. Prog. Phys.* **80**, 076501 (2017).
 [6] Y. Xia, D. Qian, D. Hsieh, L. Wray, A. Pal, H. Lin, A. Bansil, D. Grauer, Y. S. Hor, R. J. Cava, and M. Z. Hasan, *Nat. Phys.* **5**, 398 (2009).
 [7] Z.-H. Pan, E. Vescovo, A. V. Fedorov, D. Gardner, Y. S. Lee, S. Chu, G. D. Gu, and T. Valla, *Phys. Rev. Lett.* **106**, 257004 (2011).
 [8] C. Liu, G. Bian, T.-R. Chang, K. Wang, S.-Y. Xu, I. Belopolski, I. Miotkowski, H. Cao, K. Miyamoto, C. Xu, C. E. Matt, T. Schmitt, N. Alidoust, M. Neupane, H.-T. Jeng, H. Lin, A. Bansil, V. N. Strocov, M. Bissen, A. V. Fedorov, X. Xiao, T. Okuda, Y. P. Chen, and M. Z. Hasan, *Phys. Rev. B* **92**, 115436 (2015).
 [9] C. Brune, C. X. Liu, E. G. Novik, E. M. Hankiewicz, H. Buhmann, Y. L. Chen, X. L. Qi, Z. X. Shen, S. C. Zhang, and L. W. Molenkamp, *Phys. Rev. Lett.* **106**, 126803 (2011).
 [10] K. M. Dantscher, D. A. Kozlov, P. Olbrich, C. Zoth, P. Faltermeier, M. Lindner, G. V. Budkin, S. A. Tarasenko, V. V. Bel'kov, Z. D. Kvon, N. N. Mikhailov, S. A. Dvoretzky, D. Weiss, B. Jenichen, and S. D. Ganichev, *Phys. Rev. B* **92**, 165314 (2015).
 [11] L. Wu, M. Salehi, N. Koirala, J. Moon, S. Oh, and N. P. Armitage, *Science* **354**, 1124 (2016).
 [12] D. Culcer, *Phys. E (Amsterdam, Neth.)* **44**, 860 (2012).
 [13] M. Brahlek, N. Koirala, N. Bansal, and S. Oh, *Solid State Commun.* **215-216**, 54 (2015).
 [14] D. A. Kozlov, Z. D. Kvon, E. B. Olshanetsky, N. N. Mikhailov, S. A. Dvoretzky, and D. Weiss, *Phys. Rev. Lett.* **112**, 196801 (2014).

- [15] H. Maier, J. Ziegler, R. Fischer, D. Kozlov, Z. D. Kvon, N. Mikhailov, S. A. Dvoretzky, and D. Weiss, *Nat. Commun.* **8**, 2023 (2017).
- [16] D. A. Kozlov, D. Bauer, J. Ziegler, R. Fischer, M. L. Savchenko, Z. D. Kvon, N. N. Mikhailov, S. A. Dvoretzky, and D. Weiss, *Phys. Rev. Lett.* **116**, 166802 (2016).
- [17] J. Chen, H. J. Qin, F. Yang, J. Liu, T. Guan, F. M. Qu, G. H. Zhang, J. R. Shi, X. C. Xie, C. L. Yang, K. H. Wu, Y. Q. Li, and L. Lu, *Phys. Rev. Lett.* **105**, 176602 (2010).
- [18] D. Kim, S. Cho, N. P. Butch, P. Syers, K. Kirshenbaum, S. Adam, J. Paglione, and M. S. Fuhrer, *Nat. Phys.* **8**, 459 (2012).
- [19] L. Bao, L. He, N. Meyer, X. Kou, P. Zhang, Z.-g. Chen, A. V. Fedorov, J. Zou, T. M. Riedemann, T. A. Lograsso, K. L. Wang, G. Tuttle, and F. Xiu, *Sci. Rep.* **2**, 726 (2012).
- [20] S. Wolgast, Ç. Kurdak, K. Sun, J. W. Allen, D. J. Kim, and Z. Fisk, *Phys. Rev. B* **88**, 180405(R) (2013).
- [21] P. Olbrich, L. E. Golub, T. Herrmann, S. N. Danilov, H. Plank, V. V. Bel'kov, G. Mussler, C. Weyrich, C. M. Schneider, J. Kampmeier, D. Grützmacher, L. Plucinski, M. Eschbach, and S. D. Ganichev, *Phys. Rev. Lett.* **113**, 096601 (2014).
- [22] J. Tian, C. Chang, H. Cao, K. He, X. Ma, Q. Xue, and Y. P. Chen, *Sci. Rep.* **4**, 4859 (2014).
- [23] Y. Xu, I. Miotkowski, C. Liu, J. Tian, H. Nam, N. Alidoust, J. Hu, C.-K. Shih, M. Z. Hasan, and Y. P. Chen, *Nat. Phys.* **10**, 956 (2014).
- [24] R. Yoshimi, A. Tsukazaki, Y. Kozuka, J. Falson, K. S. Takahashi, J. G. Checkelsky, N. Nagaosa, M. Kawasaki, and Y. Tokura, *Nat. Commun.* **6**, 6627 (2015).
- [25] C. Li, B. de Ronde, A. Nikitin, Y. Huang, M. S. Golden, A. de Visser, and A. Brinkman, *Phys. Rev. B* **96**, 195427 (2017).
- [26] J. Ziegler, R. Kozlovsky, C. Gorini, M.-H. Liu, S. Weishäupl, H. Maier, R. Fischer, D. A. Kozlov, Z. D. Kvon, N. Mikhailov, S. A. Dvoretzky, K. Richter, and D. Weiss, *Phys. Rev. B* **97**, 035157 (2018).
- [27] A. Shuvaev, G. Astakhov, C. Brüne, H. Buhmann, L. W. Molenkamp, and A. Pimenov, *Semicond. Sci. Technol.* **27**, 124004 (2012).
- [28] A. Shuvaev, A. Pimenov, G. V. Astakhov, M. Mühlbauer, C. Brüne, H. Buhmann, and L. W. Molenkamp, *Appl. Phys. Lett.* **102**, 241902 (2013).
- [29] J. Wiedenmann, E. Liebhaber, J. Kübert, E. Bocquillon, P. Burset, C. Ames, H. Buhmann, T. M. Klapwijk, and L. W. Molenkamp, *Phys. Rev. B* **96**, 165302 (2017).
- [30] L. Muchler, H. Zhang, S. Chadov, B. Yan, F. Casper, J. Kubler, S.-C. Zhang, and C. Felser, *Angew. Chem., Int. Ed.* **51**, 7221 (2012).
- [31] B. Bradlyn, L. Elcoro, J. Cano, M. G. Vergniory, Z. Wang, C. Felser, M. I. Aroyo, and B. A. Bernevig, *Nature (London)* **547**, 298 (2017).
- [32] N. Berchenko and M. Pashkovskii, *Phys. Usp.* **119**, 223 (1976).
- [33] The HgTe diffraction peak symmetry in the x-ray spectra proves that the HgTe film is strained uniformly since any inhomogeneity would lead to a noticeable asymmetry of the peaks.
- [34] T. P. Smith, B. B. Goldberg, P. J. Stiles, and M. Heiblum, *Phys. Rev. B* **32**, 2696 (1985).
- [35] Z. D. Kvon, E. B. Olshanetsky, D. A. Kozlov, N. N. Mikhailov, and S. A. Dvoretzky, *JETP Lett.* **87**, 502 (2008).
- [36] R. Fletcher, M. Tsaousidou, T. Smith, P. T. Coleridge, Z. R. Wasilewski, and Y. Feng, *Phys. Rev. B* **71**, 155310 (2005).
- [37] A. Inhofer, S. Tchoumakov, B. A. Assaf, G. Fève, J. M. Berroir, V. Jouffrey, D. Carpentier, M. O. Goerbig, B. Plaçais, K. Bendias, D. M. Mahler, E. Bocquillon, R. Schlereth, C. Brüne, H. Buhmann, and L. W. Molenkamp, *Phys. Rev. B* **96**, 195104 (2017).
- [38] E. E. Mendez, L. Esaki, and L. L. Chang, *Phys. Rev. Lett.* **55**, 2216 (1985).